International Journal of
Molecular Sciences

MDPI

Article

Memristive Switching Characteristics in Biomaterial Chitosan-Based Solid Polymer Electrolyte for Artificial Synapse

Shin-Yi Min and Won-Ju Cho *

Department of Electronic Materials Engineering, Kwangwoon University, Chambit-kwan, B104, Nowon-gu, Seoul 01897, Korea; kkuregi1234@naver.com
* Correspondence: chowj@kw.ac.kr; Tel.: +82-2-940-5163; Fax: +82-2-943-5163

Abstract: This study evaluated the memristive switching characteristics of a biomaterial solid polymer electrolyte (SPE) chitosan-based memristor and confirmed its artificial synaptic behavior with analog switching. Despite the potential advantages of organic memristors for high-end electronics, the unstable multilevel states and poor reliability of organic devices must be overcome. The fabricated Ti/SPE-chitosan/Pt-structured memristor has stable bipolar resistive switching (BRS) behavior due to a cation-based electrochemical reaction between a polymeric electrolyte and metal ions and exhibits excellent endurance in 5×10^2 DC cycles. In addition, we achieved multilevel per cell (MLC) BRS *I-V* characteristics by adjusting the set compliance current (I_{cc}) for analog switching. The multilevel states demonstrated uniform resistance distributions and nonvolatile retention characteristics over 10^4 s. These stable MLC properties are explained by the laterally intensified conductive filaments in SPE-chitosan, based on the linear relationship between operating voltage margin ($\Delta V_{switching}$) and I_{cc}. In addition, the multilevel resistance dependence on I_{cc} suggests the capability of continuous analog resistance switching. Chitosan-based SPE artificial synapses ensure the emulation of short- and long-term plasticity of biological synapses, including excitatory postsynaptic current, inhibitory postsynaptic current, paired-pulse facilitation, and paired-pulse depression. Furthermore, the gradual conductance modulations upon repeated stimulation by 10^4 electric pulses were evaluated in high stability.

Keywords: organic memristor; chitosan; solid polymer electrolyte; electronic synapses; multilevel state

Citation: Min, S.-Y.; Cho, W.-J. Memristive Switching Characteristics in Biomaterial Chitosan-Based Solid Polymer Electrolyte for Artificial Synapse. *Int. J. Mol. Sci.* **2021**, *22*, 773. https://doi.org/10.3390/ijms22020773

Received: 19 December 2020
Accepted: 10 January 2021
Published: 14 January 2021

1. Introduction

The rapid development of electronic technology and information science requires various types of device structures, materials, and computing methods [1,2]. Memory devices are among the most essential units in electronics [3,4]. In particular, memristor-based memories have potential applications in next-generation information technology. Two-terminal metal–insulator–metal structure memristors offer significant advantages due to their geometrical simplicity, nonvolatile storage, and computations through continuous analog resistance switching in the insulator layer [5–8]. Various materials can be utilized for resistive switching (RS) layers in memristors, such as organic, inorganic, and hybrid nanocomposites [9]. Among them, bio-inspired organics such as chitosan, starch, cellulose, albumen, and gelatin are emerging materials, and numerous studies have reported RS behavior in bio-inspired organics [10–13]. Whereas the advanced electronics such as wearable, skin-attachable, and digestible smart devices should be fabricated in not only rigid substrate but, also, on flexible, stretchable, and transparent substrates [14,15]. Therefore, the solution-based low-temperature processible natural organic materials can provide versatile engineering platforms and are an interesting alternative to inorganic-based technology with biodegradability, bio-absorbability, and nontoxicity [9,16]. Nevertheless, the poor endurance, unstable long-term retention, and scarcity of states of bio-organic-based memristors must be overcome. Among various organic-based materials, chitosan electrolytes

are promising for solid polymer electrolyte (SPE)-based memristor devices due to the following advantages: chitosan is a cationic biopolymer derived from chitin extracted from shrimp or crab shells, consisting of repeating β(1,4)-linked D-glucosamine (*N*-deacetylated chitin) and *N*-acetyl-D-glucosamine units [17,18], (1) chitosan is natively insulating, but its ionic conductivity can be modulated by adding acidic solution, (2) the amine and hydroxyl groups in chitosan are extremely reactive with metal ions, (3) chitin, which is the source material of chitosan, is the second-most abundant polysaccharide in the crust, followed by cellulose, (4) chitosan is a nontoxic and biodegradable polymer, and (5) chitosan powder or flakes are soluble in diluted acetic acid solution. Therefore, chitosan has low-cost solution processability, and thin-film-formed chitosan has high transparency and flexibility by its medium molecular weight [17,19–21].

In this study, we applied a biomaterial, SPE-chitosan, to the RS layer of a two-terminal memristor device with a Ti/SPE-chitosan/Pt structure. There have been previously reported literature using chitosan as the RS layer of memristor, but without an additional powder-doping process or multilevel resistance, the properties on chitosan were not reported [9,17,19]. The interaction between the SPE and electrode can be used for cation-based electrochemical switching due to the redox reaction of mobile ions in the polymeric electrolytes [17,22]. When an electric field is applied to the electrodes of the SPE-based memristor, the electrochemical metallization (ECM) reaction strongly affects the RS phenomenon. Electrochemically reactive metal electrodes provide mobile cations, and their discharge leads to the growth of highly conductive filaments (CFs) [23]. As a result, we evaluated the stable multilevel RS, endurance, retention, and analog switching characteristics of the fabricated memristor devices without an additional doping process on chitosan. In addition, we analyzed the RS mechanism of the SPE-chitosan layer and the short- and long-term plasticity of chitosan-based SPE memristors, which are essential for synaptic calculation and information storage.

2. Results and Discussion

Figure 1a shows the optical transmittance spectra. The insets show the spectra in the visible light wavelength region (400–800 nm) for as-dried and 50 °C and 80 °C baked SPE-chitosan layers on the glass substrate and a photograph of the 80 °C baked film. The average transmittance is 90.6%, 90.7%, and 91.1% for the as-dried, 50 °C baked, and 80 °C baked SPE-chitosan layers, respectively. Thus, the transmittance increases with the baking temperature. Figure 1b presents the current–voltage (*I*-*V*) curve of the as-dried, 50 °C baked, and 80 °C baked SPE-chitosan memristor device. A DC voltage and an electrical synaptic pulse were applied to the Ti-TE (top electrode) with the Pt-BE (bottom electrode) grounded, showing that the devices exhibit typical bipolar RS (BRS) behavior. The BRS *I*-*V* characteristics were measured by applying a sequential DC bias voltage to the Ti-TE of 0 V → 2 V (compliance current (I_{cc}) of 10 mA) → −1.4 V (V_{stop}; I_{cc} of 100 mA) → 0 V with a 0.05 V step. Compared with the as-dried and 50 °C baked devices, the 80 °C baked SPE-chitosan memristor has a larger RS memory window, which is the difference in current between the high-resistance state (HRS) and low-resistance state (LRS).

Figure 2 represents the RS endurance characteristics over 5×10^2 DC cycles of the 80 °C baked SPE-chitosan memristor device. When the Ti-TE voltage is swept in the positive direction (1) in Figure 2a, the resistance state of SPE-chitosan changes from HRS to LRS, which corresponds to the set operation and the conductive ON state. Conversely, with sweeping in the negative direction (3), the resistance state changes from LRS to HRS, which corresponds to the reset operation and the conductive OFF state.

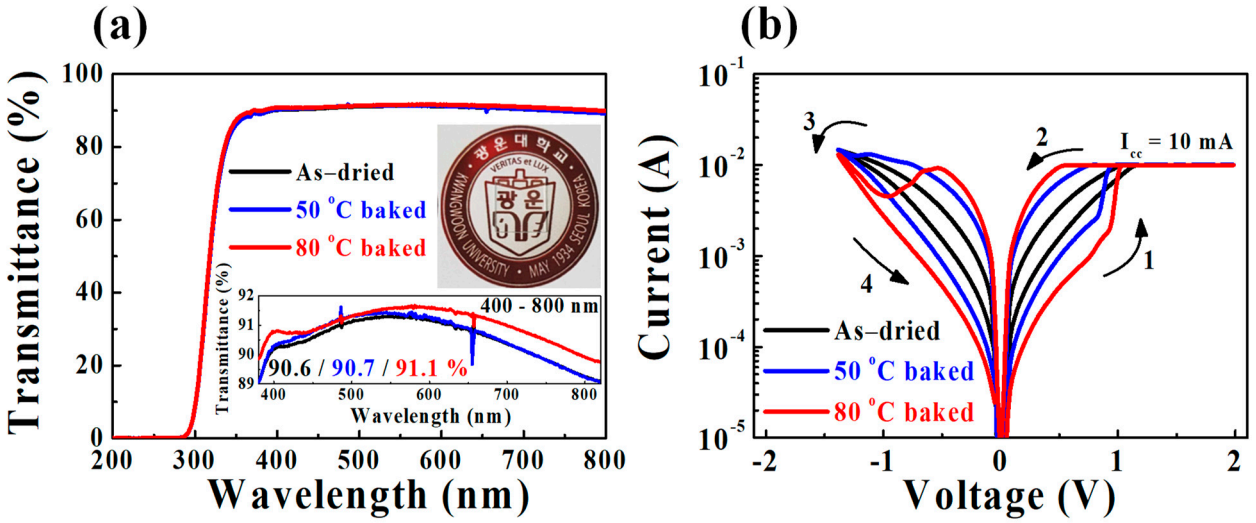

Figure 1. (**a**) Optical transmittance spectra of as-dried, 50 °C baked, and 80 °C baked solid polymer electrolyte (SPE)-chitosan layers on the glass substrate. The insets show the transmittance spectra in the visible light wavelength region (400–800 nm) and a photograph of the 80 °C baked SPE-chitosan layer. (**b**) Bipolar resistive switching (BRS) *I-V* characteristics of as-dried, 50 °C baked, and 80 °C baked SPE-chitosan memristors.

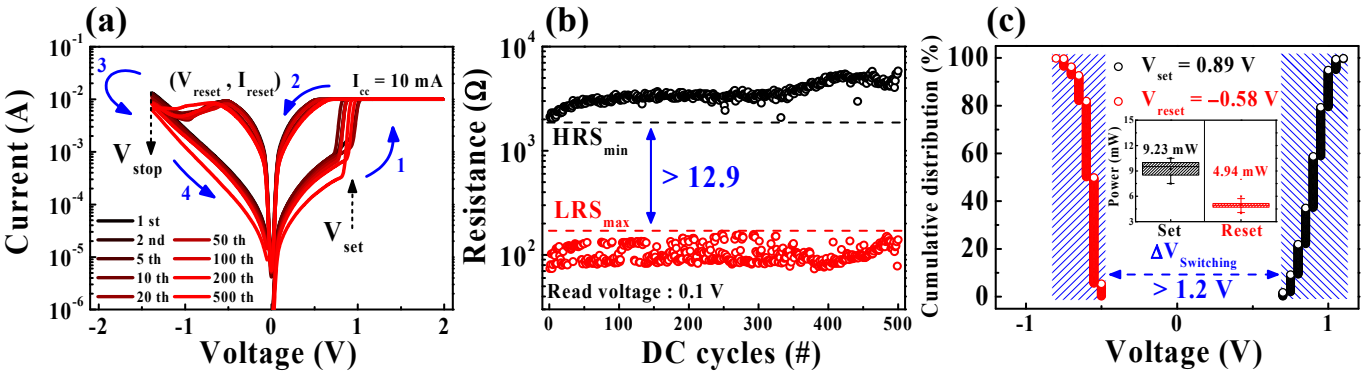

Figure 2. RS endurance characteristics for 5×10^2 DC cycles of 80 °C baked SPE-chitosan memristors. (**a**) BRS *I-V* characteristics. (**b**) Resistance values of a low-resistance state (LRS) and high-resistance state (HRS) extracted at a read voltage of 0.1 V. (**c**) Cumulative distribution of the set and reset operating voltages. The inset depicts the calculated set and reset operating powers.

In Figure 2a, it can be seen that the repetitive RS operation continuously occurs according to the voltage sweep direction. Figure 2b shows the resistance values read at 0.1 V for the LRS and HRS extracted for 5×10^2 repeated DC cycle tests. The on/off ratio of the RS window can be given as the minimum HRS (HRS_{min})/maximum LRS (LRS_{max}), where $HRS_{min}/LRS_{max} > 12.9$ was maintained without deterioration. Figure 2c presents the cumulative distribution of the set and reset operating voltages (V_{set} and V_{reset}) during 5×10^2 RS cycles. The V_{set} can be defined as the voltage at the point where the resistance state changes from HRS to LRS. On the other hand, the reset current (I_{reset}) can be defined as the peak current value when the current begins to decrease during the reset process, and the V_{reset} is the voltage corresponding to I_{reset} [24]. The inset depicts the power for the set and reset operations, calculated as $P_{set} = V_{set} \times I_{cc}$ and $P_{reset} = |V_{reset} \times I_{reset}|$, respectively. The average V_{set}, V_{reset}, P_{set}, and P_{reset} values required to accomplish set and reset operations are 0.89 V, −0.58 V, 9.23 mW, and 4.94 mW, respectively. The total operating parameters of SPE-chitosan memristor are represented in Table 1. In addition, a sufficient operating voltage margin ($\Delta V_{switching}$) larger than 1.2 V was obtained from the relationship $\Delta V_{switching} = V_{set,min} - V_{reset,max}$.

Table 1. Total operating parameters of solid polymer electrolyte (SPE)-chitosan memristor.

	Average (μ)	Standard Deviation (σ)	$\mu \pm \sigma$
Set operating voltage (V_{set})	0.89 V	0.08 V	0.89 ± 0.08 V
Set operating voltage (V_{reset})	−0.58 V	0.05 V	−0.58 ± 0.05 V
Power for set operation (P_{set})	9.23 mW	0.75 mW	9.23 ± 0.75 mW
Power for reset operation (P_{reset})	4.94 mW	0.42 mW	4.94 ± 0.42 mW

Figure 3 shows the nonvolatile multilevel per cell (MLC) characteristics of the SPE-chitosan memristor device. Nonvolatile MLC characteristics in a single memristor cell are essential to achieve a biological synaptic storage/computing system, as well as to provide a large memory capacity in the same chip area. By adjusting the I_{cc} during a set operation, the conductance of the LRS increases as the filament widens, resulting in multiple LRS levels with the same HRS level [25,26].

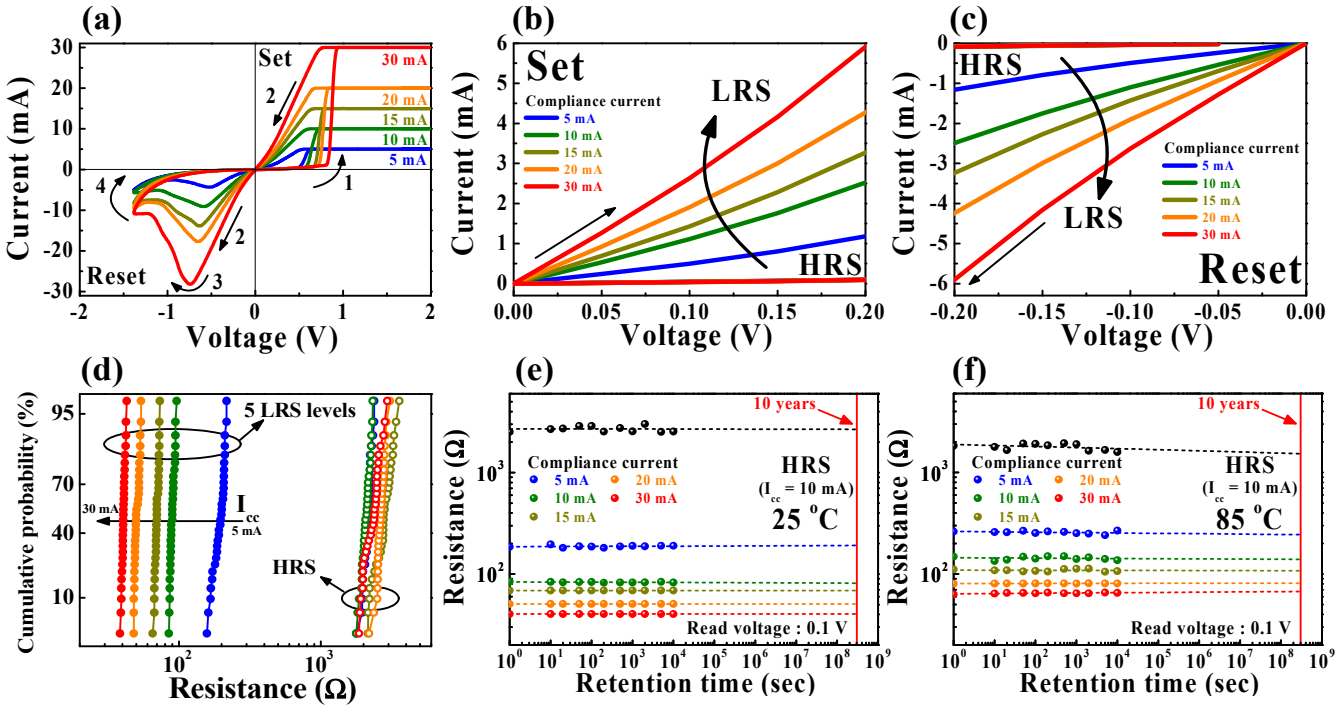

Figure 3. Multilevel per cell (MLC) characteristics of SPE-chitosan memristors. (**a**) Multilevel BRS *I-V* curves obtained by adjusting the set compliance current (I_{cc}) value from 5 to 30 mA. (**b**,**c**) The enlarged positive- and negative-voltage regions of the BRS *I-V* curves, respectively. (**d**) Cumulative probabilities of five different LRS and HRS levels during repetitive cycling. Nonvolatile retention performance of six different resistance states during 10^4 s at (**e**) room temperature (25 °C) and (**f**) a high temperature (85 °C).

Figure 3a depicts the multilevel BRS characteristics on a linear *I-V* scale. In Figure 3b,c, as the I_{cc} increases from 5 to 30 mA during the setup operation, the read current of the LRS increases, resulting in one HRS level and five LRS levels until the reset operation. Figure 3d presents the cumulative probability of multilevel resistance states for 30 cycles of repetitive switching. The open and closed symbols correspond to the HRS and LRS levels, respectively. It turns out that reliable multilevel RS operation and variability of the resistance distribution decreases with the increasing I_{cc}. The resistance values of the average (μ) ± standard deviations (σ) of the LRS are 89.89 ± 3.16 Ω for I_{cc} = 5 mA and 40.69 ± 1.03 Ω for I_{cc} = 30 mA. The narrow LRS distribution at the high I_{cc} is explained by a well-defined conductive path with thick filament diameter formation [24,27]. The total LRS resistance values of $\mu \pm \sigma$, according to the I_{cc}, are represented in Table 2.

Table 2. Total low-resistance state (LRS) resistances values of average (μ) ± standard deviations (σ), according to the I_{cc}.

Set Compliance Current (I_{cc})	**5 mA**	**10 mA**	**15 mA**	**20 mA**	**30 mA**
Average (μ)	89.89	70.01	50.69	44.90	40.69
Standard deviations (σ)	3.16	2.19	2.01	0.92	1.03
$\mu \pm \sigma$	89.89 ± 3.16	70.01 ± 2.19	50.69 ± 2.01	44.90 ± 0.92	40.69 ± 1.03

Figure 3e,f shows the nonvolatile MLC retention performance over 10^4 s at room temperature (25 °C) and a high temperature (85 °C), respectively. The retention tests for six different multilevel resistance states, including the HRS, were performed under a nondestructive read voltage of 0.1 V. All resistance states exhibited stable nonvolatile memory levels without a noticeable degradation in both the room and high-temperature conditions.

Figure 4a,b shows the voltage distribution of the set operation (V_{set}) and reset operation (V_{reset}) according to the I_{cc} and the $\Delta V_{switching}$, respectively. As the I_{cc} increases from 5 to 30 mA, the V_{set} and V_{reset} increase, resulting in a linear increase in $\Delta V_{switching}$. This multilevel characteristic can be explained by the lateral growth of the CF in the SPE-chitosan RS layer. The increase in the I_{cc} of the chitosan memristor leads to a decrease in the LRS resistance (R_{LRS}) due to CF widening, which requires a higher V_{set} to form a larger CF. On the other hand, the V_{reset} and I_{reset} increase with the increasing I_{cc}, because higher power is required to rupture a thicker filament [28–30]. Figure 4d provides a schematic of the multilevel RS operating mechanism with variation of the set I_{cc} value. The redox reaction of the mobile ions originating from the Ti-TE in the polymeric SPE-chitosan can lead to cation-based electrochemical switching. As the amine and hydroxyl groups of chitosan are extremely reactive with metal ions, the ECM reaction strongly influences the RS behavior [17,22,23,31]. When a positive bias is applied to the Ti-TE, the cation migration and discharge lead to CF growth. As the I_{cc} increases, the size of the CF path increases, resulting in a higher value of V_{set} for the enhanced electrochemical reactions. Meanwhile, in the reset process, higher values of the V_{reset} and I_{reset} are required as the I_{cc} increases, because the negative bias of the Ti-TE requires higher power to rupture the widened CF [32,33]. Figure 4c depicts the dependence of the R_{LRS} and I_{reset} on the set I_{cc}. The I_{reset} increases linearly with increasing the set I_{cc}, and the relationship between the R_{LRS} and I_{cc} was found to be $R_{LRS} \propto (I_{cc})^{-0.88}$ with a slope of -0.88 ($R^2 = 0.99$). The multilevel resistance data, well-fitted by the curve fitting, suggest the possibility of continuous analog resistance switching in SPE-chitosan memristors [26,28,29,34].

In order to investigate the mechanism of the BRS operation in the SPE-chitosan memristor, the *I-V* curves of the set operation and reset operation were plotted by double-logarithmic plotting, as shown in Figure 5. In the 0 → 2 V region of the set operation, the *I-V* curve is divided into two distinct sections: a linear relationship in the low voltage regime ($I \propto V$, blue line) and a quadratic relationship regime up to the set voltage ($I \propto V^2$, red line). When a low voltage is applied to the Ti-TE, the number of injected carriers is less than the thermally generated free charge carriers, because the electric field of SPE-chitosan is insufficient, and the *I-V* relationship follows the Ohmic law [10,19]. When a higher voltage is applied in the second regime, the injected carrier density exceeds the thermally generated carriers, and the *I-V* curve follows the trap-controlled space-charge limited conduction (SCLC) mechanism. The space charges arise from several sources: electrons injection from the electrode, dopant ionization at the interfacial depletion regions, and mobile ion accumulation at the electrode interfaces [31,35–37]. Thus, at higher voltages, the trap centers are occupied by charge carriers, and the conduction mechanism of the HRS shows an $I \propto V^2$ dependence consistent with SCLC. The insets in Figure 5 are the fitted *I-V* curves in the high-voltage region, which correspond well to the $I \propto V^2$ relationship. After the set operation, the linear *I-V* characteristic ($I \propto V$, green line) in the 2 → 0 V region indicates the formation of the filament conduction path, which is maintained until the reset operation. In the negative bias region after the reset operation (−1.4 → 0 V),

the transition between the SCLC-controlled mechanism and Ohmic conduction occurs sequentially [31,38].

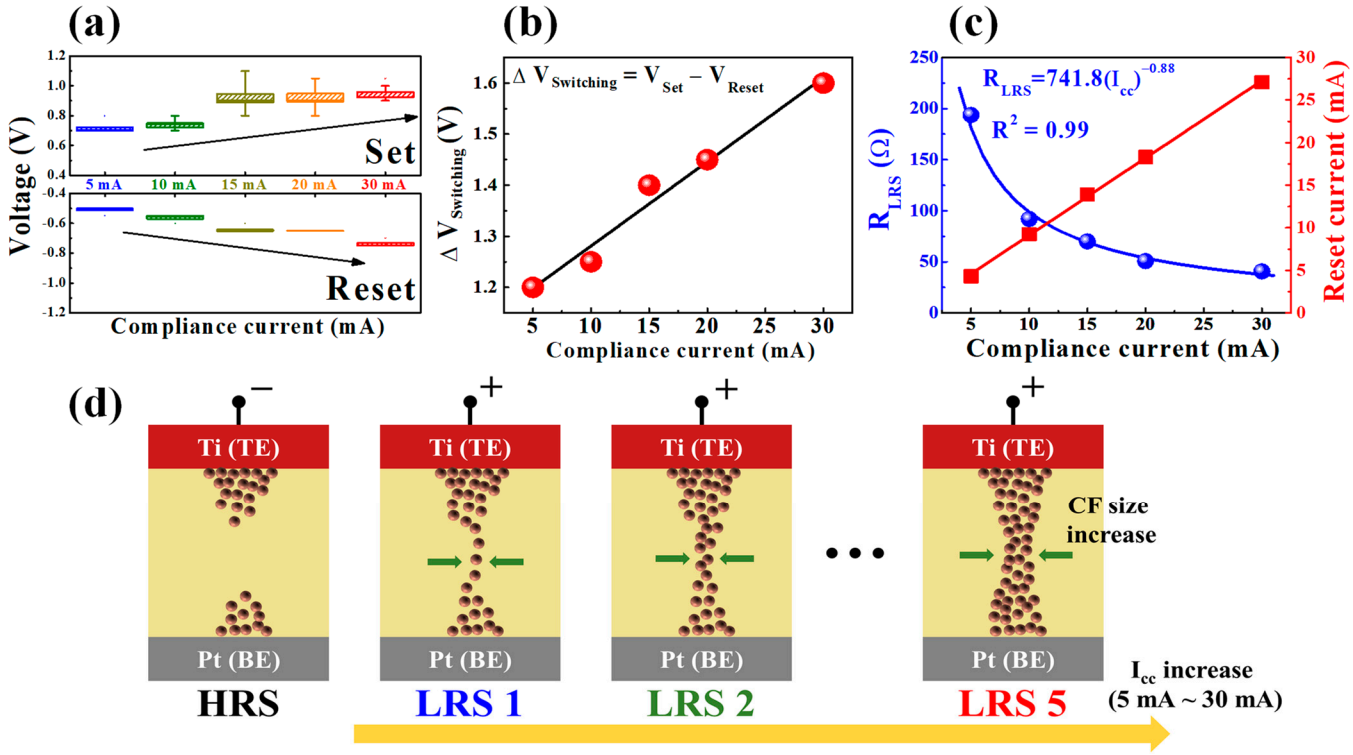

Figure 4. (**a**) Effects of the set I_{cc} value on the set operating voltage (V_{set}) and reset operating voltage (V_{reset}) distribution. (**b**) Dependence of operating voltage margin ($\Delta V_{switching}$) on the I_{cc} during repetitive cycling. (**c**) Dependence of LRS resistance (R_{LRS}) and reset current (I_{reset}) on the set I_{cc} value. (**d**) Schematic illustration of the multilevel RS operation mechanism with variations of the set I_{cc} value. TE: top electrode and BE: bottom electrode.

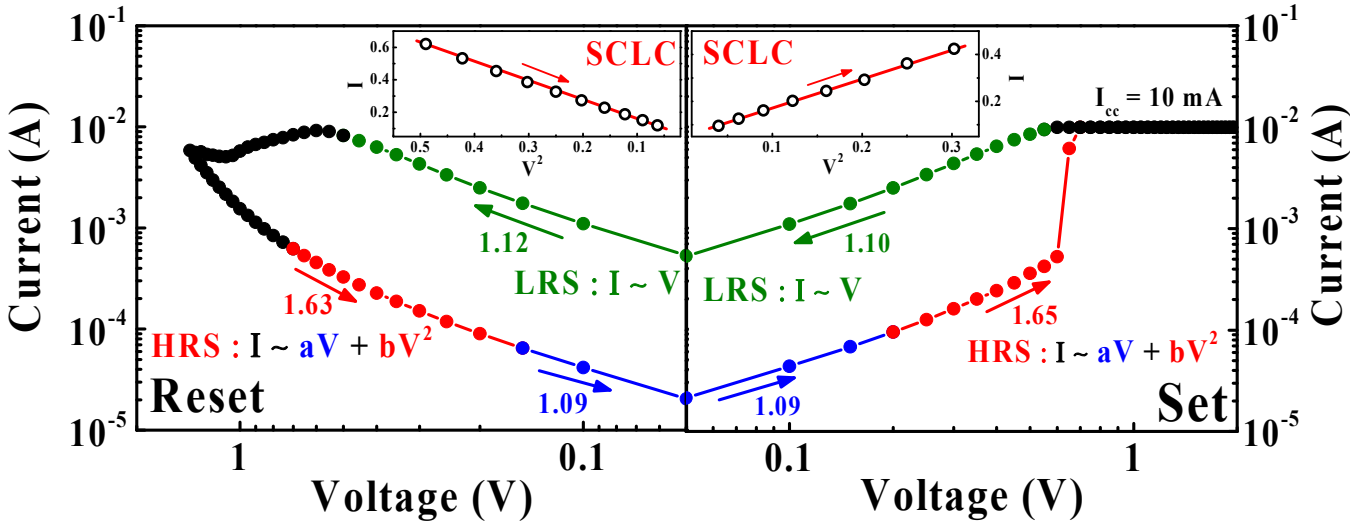

Figure 5. Double-logarithmic plots of the BRS *I-V* curves of the SPE-chitosan memristor. The blue and red lines on the HRS curve represent the linear and quadratic relations, respectively, and the green line on the LRS curve represents a linear relation. The insets are the *I-V* curves of the HRS at high voltage, which are well-fitted by the space-charge limited conduction (SCLC) mechanism.

In the biological neural system, neurons transmit information through synapses via electrical or chemical stimuli, and in-memory computing is possible according to the synap-

tic plasticity, which is the strength of the connection between neurons and plays the most important role in the memory function of the brain. Figure 6a provides a schematic diagram of a simplified biological synapse, and Figure 6b illustrates a typical learning/memory model suggested by Atkinson and Shiffrin [39]. According to this model, most of the unattended incoming information is quickly lost in the brain, but the information humans focus on is temporarily stored as short-term memory (STM). Afterward, when the maintenance rehearsal of stimuli is triggered, STM is transferred into long-term memory (LTM). This basic principle of neurons for learning/memory is consistent with the RS phenomenon of the memristor, and both are based on synaptic plasticity, which can be modulated by the stimulus history [40,41].

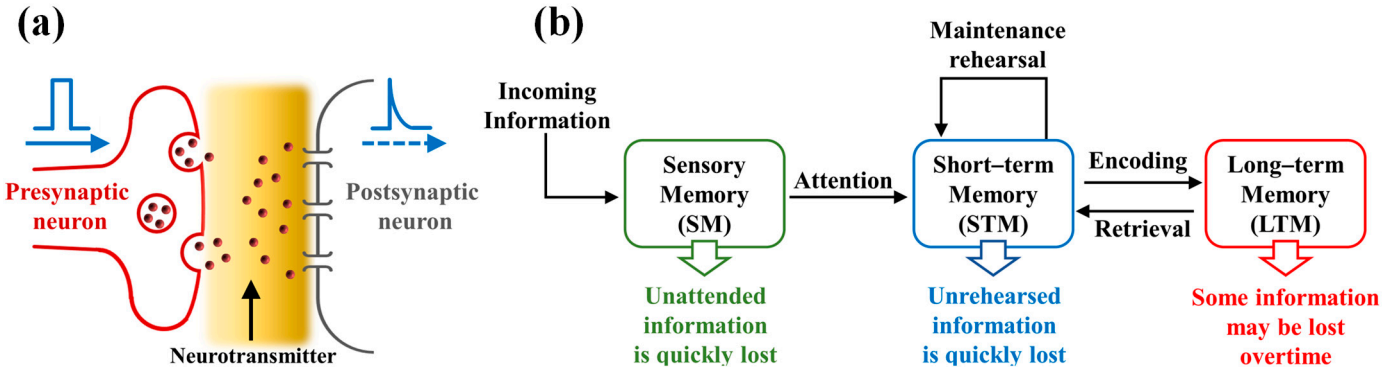

Figure 6. (**a**) Schematic diagram of a simplified biological synapse. (**b**) A typical learning and memory model describing short-term memory (STM) and long-term memory (LTM) behaviors in the brain.

The paired-pulse facilitation (PPF) and paired-pulse depression (PPD) behaviors are considered typical short-term synaptic plasticity characteristics crucial for both excitatory and inhibitory responses between adjacent synaptic connections. As a function of the interval time (Δt) between two consecutive presynaptic spikes, the second synaptic spike after the first spike evokes a larger excitatory postsynaptic current (EPSC) for PPF or a smaller inhibitory postsynaptic current (IPSC) for PPD. Figure 7a,b demonstrates the EPSC and IPSC properties triggered by the paired presynaptic spikes of positive pulses (PPF; 1 V, 50 ms) and negative pulses (PPD; −1 V, 50 ms) with Δt = 70 ms, respectively.

In the PPF response, the second PSC peak (A_2)/first PSC peak (A_1) is >1, whereas, in the PPD response, the A_2/A_1 is <1. Figure 7c summarizes the indices of the PPF and PPD responses as functions of the Δt of the paired pulses in terms of A_2/A_1 (%). When the Δt becomes sufficiently short (Δt = 60 ms), the response index exponentially increases to ~123% for PPF and significantly decreases to ~79% for PPD. On the other hand, when the Δt becomes sufficiently long (Δt > 2000 ms), both the PPF and PPD response indices gradually decrease, saturating at about ~100% and mimicking the biological synaptic response [42,43]. In addition, the fitting curves were obtained using the following double-exponential decay function. It can be seen that the measured PPF and PPD indices (closed circles) are well-fitted by the double-exponential decay function (solid lines). The extracted relaxation time constants τ_1 and τ_2 are 40.4 ms and 593.2 ms for the PPF response, and 60.3 ms and 986.6 ms for the PPD response, respectively. The time scales of these fitting results are similar to those of typical biological synapses, which can be subdivided into rapid and slow phases lasting tens and hundreds of milliseconds, respectively [44]. The total response parameters in the PPF and PPD behaviors of SPE-chitosan memristor are represented in Table 3.

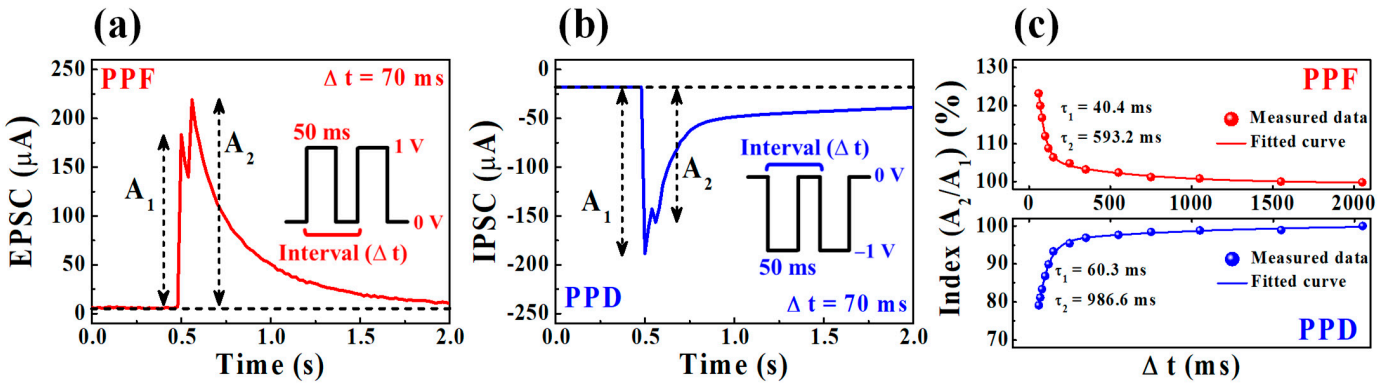

Figure 7. (**a**) Paired-pulse facilitation (PPF) and (**b**) paired-pulse depression (PPD) emulations of SPE-chitosan memristors (interval time (Δt) = 70 ms). (**c**) The PPF and PPD index (the second postsynaptic current peak/the first postsynaptic current peak (A_2/A_1) in %) as a function of the Δt in paired presynaptic spikes. The closed circles are the measured data, and the solid line is the result of fitting by the double-exponential decay function.

Table 3. Total response parameters in the paired-pulse facilitation (PPF) and paired-pulse depression (PPD) behaviors of SPE-chitosan memristor. τ_1 and τ_2 are the relaxation time constants, and Δt is the time interval.

	Index (Δt = 60 ms)	Index (Δt > 2000 ms)	τ_1	τ_2
PPF	~123%	~100%	40.4 ms	593.2 ms
PPD	~79%	~100%	60.3 ms	986.6 ms

Meanwhile, the long-term plasticity of individual memristors facilitates the large-scale processing of information. Moreover, the RS behavior of filamentary memristors has quite analogous synaptic weight changes between adjacent synaptic connections. Therefore, CF-based memristors are considered as a suitable candidate for biological neuromorphic systems [45–47]. To investigate the transition from analog filamentary switching in the SPE-chitosan memristors, we evaluated the conductance modulation of the potentiation/depression behavior through presynaptic pulses, as depicted in Figure 8. Figure 8a exhibits a consecutive increase/decrease in conductivity with stimulation by 100 repeated pulses (one cycle) in the SPE-chitosan memristor, and the insets show the pulse schemes for potentiation, depression, and read behaviors. One cycle consists of 50 potentiation pulses and 50 depression pulses, in which the pulse conditions used for potentiation/depression were 1.2 V/10 ms and −1.6 V/10 ms, respectively. We performed 100 cycles of the conductance modulation operation using a total of 10^4 pulses, as shown in Figure 8b. The conductance modulation, in the dynamic range of ~2 mS, was well-modulated and almost unchanged over the 100-cycles test. In addition, to clarify the difference in the DC *I-V* curve before and after the cycling test, we compared the BRS characteristics and resistance values of the initial, after 100-, after 200-, and after 300-cycle tests in Figure 8c,d. As a result, it was verified that there was little change without remarkable degradation in the DC *I-V* curve characteristics and resistance values of HRS and LRS after repeated pulse-induced cycling tests in the SPE-chitosan memristor.

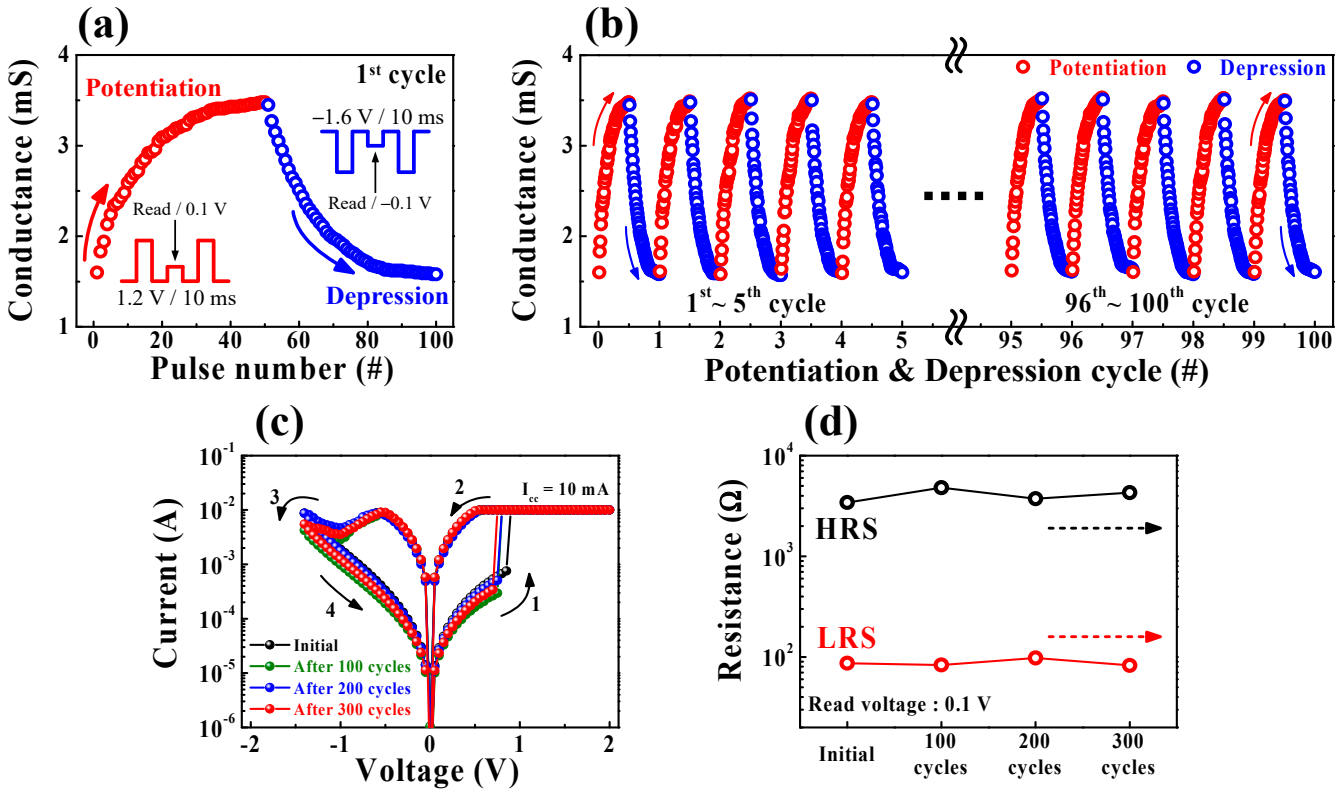

Figure 8. Potentiation/depression behaviors of SPE-chitosan memristors obtained by repeated presynaptic pulses of 1.2 V and −1.6 V with 10-ms widths, respectively. Conductance modulation in (**a**) one-cycle (insets show the potentiation, depression, and read pulse schemes) and (**b**) 100-cycle tests with stimulation by 10^4 pulses. (**c**) BRS *I-V* characteristics and (**d**) resistance values of the initial, after 100-, after 200-, and after 300-cycle tests.

3. Experimental

3.1. Materials

p-type Si wafer (resistivity range between 1–10 Ω·cm, LG SILTRON Inc., Gumi, Korea). Ti pellet (purity > 99.999%, TFN, Seoul, Korea). Pt pellet (purity > 99.95%, TFN, Korea). Chitosan powder (derived from shrimp shell, medium molecular weight: 190–310 kDa, deacetylation degree > 75%, Sigma Aldrich, Seoul, Korea). Acetic acid solution (purity > 99%, Sigma Aldrich).

3.2. Chitosan Solution Preparation Procedure

The biomaterial chitosan electrolytic solution was prepared by the dissolution process of chitosan powder and acetic acid mixture. The chitosan powder derived from a shrimp shell of medium molecular weight (deacetylation degree > 75%, Sigma Aldrich) was dissolved (2 wt%) in an acetic acid solution (purity > 99%, Sigma Aldrich) diluted (2 wt%) with deionized water. Subsequently, the solution was mixed using a constant magnetic stirring system at 800 rpm for 6 h at 50 °C. Finally, the resultant solution was filtered through a 5-μm pore size polytetrafluoroethylene syringe filter (Whatman International Ltd., Maidstone, UK) to remove impurities.

3.3. SPE-Chitosan Memristor Devices Fabrication

A 300-nm-thick thermally oxidized p-type Si wafer ((100) planes silicon wafer) was cleaned by a standard Radio Corporation of America cleaning process. To form the bottom electrode (BE), a 10-nm-thick Ti adhesive layer and 100-nm-thick Pt layer were sequentially deposited on the substrate using an electron beam (E-beam) deposition system. The chitosan electrolytic solution was spin-coated on the BE at 6000 rpm for 30 s. The coated film was then dried under ambient conditions for 24 h and then baked at 80 °C for 10 min in a

convection oven system to form a uniform SPE-chitosan layer with a thickness of 150 nm. Finally, a 100-nm-thick Ti top electrode (TE) with a diameter of 200 µm was deposited on the SPE-chitosan RS layer using an E-beam evaporation system and a shadow mask. Figure 9a shows a schematic diagram of a fabricated two-terminal SPE-chitosan memristor device with a Ti/SPE-chitosan/Pt structure, and Figure 9b,c provides optical microscope images with magnifications of 150× and 300×, respectively.

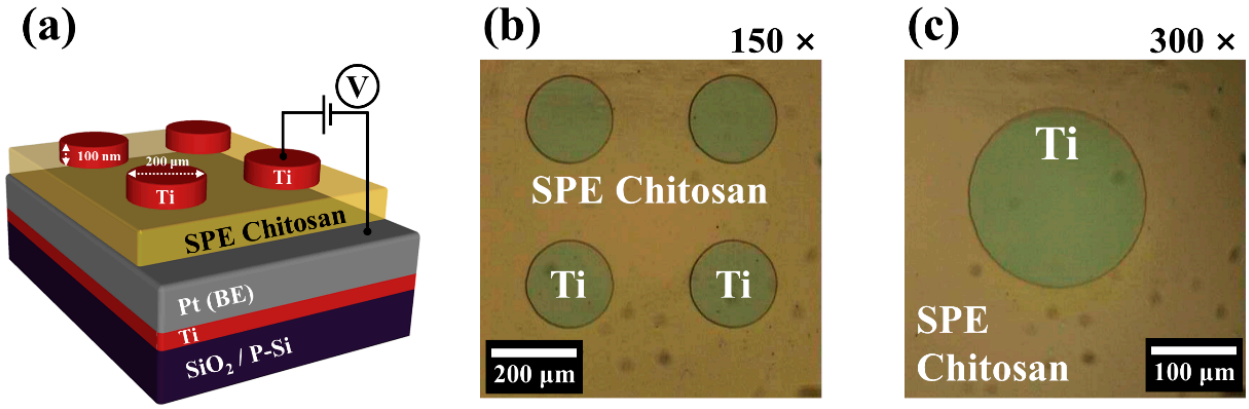

Figure 9. (**a**) Schematic diagram of the SPE-chitosan memristors (Ti/SPE-chitosan/Pt) and optical microscope images with magnifications of (**b**) 150× and (**c**) 300×.

3.4. Characterization of SPE-Chitosan Memristor Devices

The memristive switching and electrical synaptic behaviors of the fabricated SPE-chitosan memristor were analyzed using an Agilent 4156B Precision Semiconductor Parameter Analyzer (Hewlett-Packard Co., Palo Alto, CA, USA). The device was placed on a two-point probe station system in a dark box to avoid light and electrical noise. To investigate the synaptic operation, electrical pulses were applied with an Agilent 8110A Pulse Generator (Hewlett-Packard Co., USA). In addition, the optical transmittance of the SPE-chitosan layer was measured in the wavelength range of 190–1100 nm using an Agilent 8453 ultraviolet-visible spectrophotometer (Hewlett-Packard Co., USA). The optical microscope image of the fabricated SPE-chitosan memristor was analyzed with magnifications of 150 × and 300 × by using an SV−55 Microscope System (SOMETECH, Seoul, Korea).

3.5. Double-Exponential Decay Function

The PPF and PPD response indices were fitted by using the following double-exponential decay function depicted:

$$F = C_1 exp(-\Delta t/\tau_1) + C_2 exp(-\Delta t/\tau_2) \quad (1)$$

where C_1 and C_2 are the initial facilitation magnitudes, and τ_1 and τ_2 are the relaxation time constants of the respective phases. The fitting procedures were carried out by using the OriginPro 8.5 software program.

4. Conclusions

We evaluated the memristive switching characteristics of a biomaterial SPE-chitosan-based memristor and demonstrated the possibility of artificial synaptic behavior with analog switching. The solution-derived SPE-chitosan layer displayed uniform thickness and high transparency in the visible light region. The SPE-chitosan memristor showed stable BRS behavior through a cation-based electrochemical reaction between a polymeric electrolyte and metal ions and exhibited excellent endurance in 5×10^2 DC cycles. In addition, the nonvolatile MLC characteristics with five different LRS and one HRS were achieved by adjusting the set I_{cc} value. These multilevel states with uniform resistance

distributions were stably maintained over a retention time of 10^4 s in both room and high-temperature conditions. As the MLC properties are influenced by the lateral growth of CFs in the SPE-chitosan layer, the $\Delta V_{switching}$ and I_{reset} have linear dependences on the set I_{cc} value. Accordingly, the multilevel resistance suggests the feasibility of continuous analog resistance switching in the SPE-chitosan memristors as an electronic synapse. Furthermore, it was demonstrated that chitosan-based SPE artificial synapses ensure the emulation of short- and long-term plasticity of biological synapses. In addition to the EPSC, IPSC, PPF, and PPD, the conductivity modulation with stimulation by 10^4 repeated pulses (dynamic range of ~2 mS) was also reliably evaluated. Therefore, this nontoxic, biodegradable biomaterial SPE-chitosan memristor with high transparency and low-cost solution processability is expected to have potential applications in in-memory analog computing in artificial intelligence processes by offering a versatile electronic platform.

Author Contributions: Conceptualization, S.-Y.M. and W.-J.C.; investigation, S.-Y.M. and W.-J.C. —original draft preparation, S.-Y.M. and W.-J.C.; writing—review and editing, S.-Y.M. and W.-J.C.; supervision, W.-J.C.; project administration, W.-J.C.; funding acquisition, W.-J.C. All authors have read and agreed to the published version of the manuscript.

Funding: The present research was conducted with the research grant of Kwangwoon University in 2020 and was supported by a National Research Foundation of Korea (NRF) grant funded by the Korean government (MIST) (No. 2020R1A2C1007586).

Conflicts of Interest: The authors declare no conflict of interest.

Abbreviations

BE	Bottom electrode
BRS	Bipolar resistive switching
CFs	Conductive filaments
E-beam	Electron beam
ECM	Electrochemical metallization
EPSC	Excitatory post-synaptic current
HRS	High-resistance state
I_{cc}	Compliance current
IPSC	Inhibitory post-synaptic current
LRS	Low-resistance state
LTM	Long-term memory
MLC	Multi-level per cell
PPD	Paired-pulse depression
PPF	Paired-pulse facilitation
RS	Resistive switching
SCLC	Space-charge-limited conduction
SPE	Solid polymer electrolyte
STM	Short-term memory
TE	Top electrode
V_{reset}	Reset operating voltage
V_{set}	Set operating voltage

References

1. Lou, Z.; Wang, L.; Jiang, K.; Wei, Z.; Shen, G. Reviews of wearable healthcare systems: Materials, devices and system integration. *Mater. Sci. Eng. R Rep.* **2020**, *140*, 100523. [CrossRef]
2. Zhang, Z.; Wang, Z.; Shi, T.; Bi, C.; Rao, F.; Cai, Y.; Zhou, P. Memory materials and devices: From concept to application. *InfoMat* **2020**, *2*, 261–290. [CrossRef]
3. Gupta, V.; Kapur, S.; Saurabh, S.; Grover, A. Resistive random access memory: A review of device challenges. *IETE Tech. Rev.* **2020**, *37*, 377–390. [CrossRef]
4. Banerjee, W. Challenges and applications of emerging nonvolatile memory devices. *Electronics* **2020**, *9*, 1029. [CrossRef]
5. Khalid, M. Review on various memristor models, characteristics, potential applications, and future works. *Trans. Electr. Electron. Mater.* **2019**, *20*, 289–298. [CrossRef]

6. Li, Y.; Wang, Z.; Midya, R.; Xia, Q.; Yang, J.J. Review of memristor devices in neuromorphic computing: Materials sciences and device challenges. *J. Phys. D Appl. Phys.* **2018**, *51*, 503002. [CrossRef]
7. Chang, T.C.; Chang, K.C.; Tsai, T.M.; Chu, T.J.; Sze, S.M. Resistance random access memory. *Mater. Today* **2016**, *19*, 254–264. [CrossRef]
8. Park, S.; Noh, J.; Choo, M.L.; Sheri, A.M.; Chang, M.; Kim, Y.B.; Kim, C.J.; Jeon, M.; Lee, B.G.; Lee, B.H.; et al. Nanoscale RRAM–based synaptic electronics: Toward a neuromorphic computing device. *Nanotechnology* **2013**, *24*, 384009. [CrossRef]
9. Raeis-Hosseini, N.; Lee, J.S. Resistive switching memory using biomaterials. *J. Electroceramics* **2017**, *39*, 223–238.
10. Raeis-Hosseini, N.; Lee, J.S. Controlling the resistive switching behavior in starch–based flexible biomemristors. *ACS Appl. Mater. Interfaces* **2016**, *8*, 7326–7332. [CrossRef]
11. Rananavare, A.P.; Kadam, S.J.; Prabhu, S.V.; Chavan, S.S.; Anbhule, V.; Dongale, T.D. Organic non–volatile memory device based on cellulose fibers. *Mater. Lett.* **2018**, *232*, 99–102. [CrossRef]
12. Chen, Y.C.; Yu, H.C.; Huang, C.Y.; Chung, W.L.; Wu, S.L.; Su, Y.K. Nonvolatile bio–memristor fabricated with egg albumen film. *Sci. Rep.* **2015**, *5*, 10022. [CrossRef] [PubMed]
13. Chang, Y.C.; Wang, Y.H. Resistive switching behavior in gelatin thin films for nonvolatile memory application. *ACS Appl. Mater. Interfaces* **2014**, *6*, 5413–5421. [CrossRef] [PubMed]
14. Li, Y.; Qian, Q.; Zhu, X.; Li, Y.; Zhang, M.; Li, J.; Zhang, Q. Recent advances in organic-based materials for resistive memory applications. *InfoMat* **2020**, *2*, 995–1033. [CrossRef]
15. Xia, Y.; He, Y.; Zhang, F.; Liu, Y.; Leng, J. A review of shape memory polymers and composites: Mechanisms, materials, and applications. *Adv. Mater.* **2020**, 2000713. [CrossRef] [PubMed]
16. Kim, D.H.; Viventi, J.; Amsden, J.J.; Xiao, J.; Vigeland, L.; Kim, Y.S.; Blanco, J.A.; Panilaitis, B.; Frechette, E.S.; Contreras, D.; et al. Dissolvable films of silk fibroin for ultrathin conformal bio–integrated electronics. *Nat. Mater.* **2010**, *9*, 511–517. [CrossRef] [PubMed]
17. Raeis Hosseini, N.; Lee, J.S. Resistive switching memory based on bioinspired natural solid polymer electrolytes. *ACS Nano* **2015**, *9*, 419–426. [CrossRef]
18. Koev, S.T.; Dykstra, H.; Luo, X.; Rubloff, G.W.; Bentley, W.E.; Payne, G.F.; Ghodssi, R. Chitosan: An integrative biomaterial for lab-on-a-chip devices. *Lab Chip* **2010**, *10*, 3026–3042. [CrossRef]
19. Hosseini, N.R.; Lee, J.S. Biocompatible and flexible chitosan-based resistive switching memory with magnesium electrodes. *Adv. Funct. Mater.* **2015**, *25*, 5586–5592. [CrossRef]
20. Jiang, J.; Kuroda, M.A.; Ahyi, A.C.; Isaacs-Smith, T.; Mirkhani, V.; Park, M.; Dhar, S. Chitosan solid electrolyte as electric double layer in multilayer MoS_2 transistor for low-voltage operation. *Phys. Status Solidi* **2015**, *212*, 2219–2225. [CrossRef]
21. Liu, Y.H.; Zhu, L.Q.; Feng, P.; Shi, Y.; Wan, Q. Freestanding artificial synapses based on laterally proton-coupled transistors on chitosan membranes. *Adv. Mater.* **2015**, *27*, 5599–5604. [CrossRef] [PubMed]
22. Wu, S.; Tsuruoka, T.; Terabe, K.; Hasegawa, T.; Hill, J.P.; Ariga, K.; Aono, M. A polymer-electrolyte-based atomic switch. *Adv. Funct. Mater.* **2011**, *21*, 93–99. [CrossRef]
23. Waser, R.; Dittmann, R.; Staikov, G.; Szot, K. Redox-based resistive switching memories–nanoionic mechanisms, prospects, and challenges. *Adv. Mater.* **2009**, *21*, 2632–2663. [CrossRef]
24. Wu, M.C.; Jang, W.Y.; Lin, C.H.; Tseng, T.Y. A study on low–power, nanosecond operation and multilevel bipolar resistance switching in $Ti/ZrO_2/Pt$ nonvolatile memory with 1T1R architecture. *Semicond. Sci. Technol.* **2012**, *27*, 065010. [CrossRef]
25. Ielmini, D. Resistive switching memories based on metal oxides: Mechanisms, reliability and scaling. *Semicond. Sci. Technol.* **2016**, *31*, 063002. [CrossRef]
26. Prakash, A.; Park, J.; Song, J.; Woo, J.; Cha, E.J.; Hwang, H. Demonstration of low power 3–bit multilevel cell characteristics in a TaO_x–based RRAM by stack engineering. *IEEE Electron Device Lett.* **2014**, *36*, 32–34. [CrossRef]
27. Bousoulas, P.; Stathopoulos, S.; Tsialoukis, D.; Tsoukalas, D. Low–power and highly uniform 3–b multilevel switching in forming free TiO_{2-x}-based RRAM with embedded Pt nanocrystals. *IEEE Electron Device Lett.* **2016**, *37*, 874–877. [CrossRef]
28. Prakash, A.; Hwang, H. Multilevel cell storage and resistance variability in resistive random access memory. *Phys. Sci. Rev.* **2016**, *1*. [CrossRef]
29. Prakash, A.; Park, J.S.; Song, J.; Lim, S.J.; Park, J.H.; Woo, J.; Cha, E.; Hwang, H. Multi–state resistance switching and variability analysis of HfO_x based RRAM for ultra–high density memory applications. In Proceedings of the 2015 International Symposium on Next-Generation Electronics (ISNE), Taipei, Taiwan, 4–6 May 2015; pp. 1–2.
30. Ambrogio, S.; Balatti, S.; Cubeta, A.; Calderoni, A.; Ramaswamy, N.; Ielmini, D. Understanding switching variability and random telegraph noise in resistive RAM. In Proceedings of the2013 IEEE International Electron Devices Meeting, Washington, DC, USA, 9–11 December 2013; pp. 31–35.
31. Tran, K.M.; Do, D.P.; Thi, K.H.T.; Pham, N.K. Influence of top electrode on resistive switching effect of chitosan thin films. *J. Mater. Res.* **2019**, *34*, 3899–3906. [CrossRef]
32. Ambrosi, E.; Bricalli, A.; Laudato, M.; Ielmini, D. Impact of oxide and electrode materials on the switching characteristics of oxide ReRAM devices. *Faraday Discuss.* **2019**, *213*, 87–98. [CrossRef]
33. Bricalli, A.; Ambrosi, E.; Laudato, M.; Maestro, M.; Rodriguez, R.; Ielmini, D. Resistive switching device technology based on silicon oxide for improved ON–OFF ratio—part I: Memory devices. *IEEE Trans. Electron Dev.* **2018**, *65*, 115–121. [CrossRef]

34. Long, B.; Li, Y.; Jha, R. Switching characteristics of Ru/HfO_2/TiO_{2-x}/Ru RRAM devices for digital and analog nonvolatile memory applications. *IEEE Electron Device Lett.* **2012**, *33*, 706–708. [CrossRef]
35. Lin, W.P.; Liu, S.J.; Gong, T.; Zhao, Q.; Huang, W. Polymer-based resistive memory materials and devices. *Adv. Mater.* **2014**, *26*, 570–606. [PubMed]
36. Mondal, S.; Her, J.L.; Chen, F.H.; Shih, S.J.; Pan, T.M. Improved resistance switching characteristics in Ti–doped Yb_2O_3 for resistive nonvolatile memory devices. *IEEE Electron Device Lett.* **2012**, *33*, 1069–1071. [CrossRef]
37. Feng, P.; Chen, C.; Wang, Z.S.; Yang, Y.C.; Yang, J.; Zeng, F. Nonvolatile resistive switching memories–characteristics, mechanisms and challenges. *Prog. Nat. Sci. Mater. Int.* **2010**, *20*, 1–15.
38. Chiu, F.C. A review on conduction mechanisms in dielectric films. *Adv. Mater. Sci. Eng.* **2014**, *2014*, 578168. [CrossRef]
39. Atkinson, R.C.; Shiffrin, R.M. Human memory: A proposed system and its control processes. *Psychol. Learn. Motiv.* **1968**, *2*, 89–195.
40. Bi, G.Q.; Poo, M.M. Synaptic modifications in cultured hippocampal neurons: Dependence on spike timing, synaptic strength, and postsynaptic cell type. *J. Neurosci.* **1998**, *18*, 10464–10472. [CrossRef]
41. McGaugh, J.L. Memory—-A century of consolidation. *Science* **2000**, *287*, 248–251. [CrossRef]
42. Zhao, J.; Zhou, Z.; Zhang, Y.; Wang, J.; Zhang, L.; Li, X.; Zhao, M.; Wang, H.; Pei, Y.; Zhao, Q.; et al. An electronic synapse memristor device with conductance linearity using quantized conduction for neuroinspired computing. *J. Mater. Chem. C* **2019**, *7*, 1298–1306.
43. Majumdar, S.; Tan, H.; Qin, Q.H.; van Dijken, S. Energy-efficient organic ferroelectric tunnel junction memristors for neuromorphic computing. *Adv. Electron. Mater.* **2019**, *5*, 1800795. [CrossRef]
44. Zucker, R.S.; Regehr, W.G. Short–term synaptic plasticity. *Ann. Rev. Physiol.* **2002**, *64*, 355–405. [CrossRef] [PubMed]
45. Lv, Z.; Zhou, Y.; Han, S.T.; Roy, V.A.L. From biomaterial–based data storage to bio–inspired artificial synapse. *Mater. Today* **2018**, *21*, 537–552. [CrossRef]
46. Sun, W.; Gao, B.; Chi, M.; Xia, Q.; Yang, J.J.; Qian, H.; Wu, H. Understanding memristive switching via in situ characterization and device modeling. *Nat. Commun.* **2019**, *10*, 3453. [CrossRef] [PubMed]
47. Wang, T.Y.; Meng, J.L.; He, Z.Y.; Chen, L.; Zhu, H.; Sun, Q.Q.; Ding, S.J.; Zhang, D.W. Atomic layer deposited $Hf_{0.5}Zr_{0.5}O_2$–based flexible memristor with short/long–term synaptic plasticity. *Nanoscale Res. Lett.* **2019**, *14*, 102. [CrossRef]